JOURNAL OF GEOPHYSICAL RESEARCH: OCEANS, VOL. 118, 3737–3751, doi:10.1002/jgrc.20261, 2013

Creation and tidal advection of a cold salinity front in Storfjorden: 2. Supercooling induced by turbulent mixing of cold water

Miles G. McPhee,[1] Ragnheid Skogseth,[2] Frank Nilsen,[2,3] and Lars H. Smedsrud[4]

Received 13 December 2012; revised 19 March 2013; accepted 29 May 2013; published 1 August 2013.

[1] Measurements near the edge of fast ice in Freemansundet, Svalbard, reveal mixing processes associated with tidal advection of a sharp front in salinity, including possible supercooling induced by double diffusion in a fully turbulent water column. The front translated back and forth with the semidiurnal tide between an area of mobile (drifting) ice in Storfjorden proper, and the narrow sound covered by fast ice. Water on each side of the front was near its salinity-determined freezing temperature. Instruments deployed about 400 m into the sound from the fast ice edge measured current, temperature, conductivity, and turbulence quantities through several tidal cycles. Turbulence data illustrate that as the steep horizontal salinity (density) gradient advected past the measurement site, vertical shear near the fast-ice base induced marked flood/ebb asymmetry in turbulent mixing. As fresher water entered the sound on the flood phase, inward transport of denser water near the upper boundary was retarded, leading to statically unstable conditions and enhanced turbulence. The opposite occurred during ebb tide, as denser water underran lighter. Transient episodes of supercooling accompanied frontal passage on both flood and ebb phases. The most likely explanation for a zone of supercooled water within the strongly mixed frontal region is that during mixing of fresher, slightly warmer (but still at freezing) water from outside with saltier, colder water in the sound, the former constituent lost heat faster than gaining salt. This interpretation (differing turbulent diffusivities for heat and salt) challenges strict application of Reynolds analogy for highly turbulent shear flow.

Citation: McPhee, M. G., R. Skogseth, F. Nilsen, and L. H. Smedsrud (2013), Creation and tidal advection of a cold salinity front in Storfjorden: 2. Supercooling induced by turbulent mixing of cold water, *J. Geophys. Res. Oceans*, *118*, 3737–3751, doi:10.1002/jgrc.20261.

1. Background

[2] One component of the 2007 Storfjorden project described in a companion paper [*Skogseth et al*., 2013] was measurement of mean and turbulent flow properties under fast (stationary) ice near the mouth of Freemansundet (FMS), a narrow sound separating Edgeøya and Barentsøya in the eastern part of the Svalbard Archipelago. Tidal flow in the sound was relatively energetic, comprising a nearly rectilinear tidal oscillation with amplitude of about 0.8 m s^{-1} superimposed on residual flow of about 0.12 m s^{-1} into the sound (i.e., to the northeast from Storfjorden proper) [see Figure 1 in *Skogseth et al*., 2013]. A notable feature of the flood/ebb cycle was back-and-forth advection of a sharp salinity front past our instruments, with fresher, slightly warmer water from outside replacing saltier, colder water on the flood, and vice versa on the ebb. As shown later, in the Eulerian frame of our instrument site, the tidally varying component of salinity appeared as a rectified wave with peak-to-peak excursion of about 0.4 on the practical salinity scale (hereafter expressed as practical salinity units, psu).

[3] At cold temperatures, salinity controls density. Advection of a horizontal salinity gradient past a solid surface thus provides a mechanism for altering the vertical static stability of the water column, as shear induced by turbulent stress retards flow near the boundary. Consequently, when salinity is decreasing (flood), we expect statically unstable conditions (lighter water underrunning heavier) and the opposite effect on the ebb. *Crawford et al*. [1999] reported measurements from Barrow Strait, NWT, showing a sevenfold difference in turbulence scale and eddy viscosity during tidal advection of a salinity gradient under fast ice, with considerably higher drag when salinity was decreasing. The phenomenon is related to a similar effect seen in open estuaries, termed tidal straining [*Rippeth et al*., 2001].

[4] Of particular interest during the FMS measurements was intermittent appearance of what we interpret as supercooled water (water in liquid state at temperatures below

Companion to *Skogseth et al.* [2013] doi:10.1002/jgrc.20231.

[1]McPhee Research Co., Naches, Washington, USA.
[2]Department of Arctic Geophysics, The University Centre in Svalbard, Longyearbyen, Norway.
[3]Geophysical Institute, University of Bergen, Bergen, Norway.
[4]Uni Research, Bjerknes Centre for Climate Research, Bergen, Norway.

Corresponding author: R. Skogseth, The University Centre in Svalbard, PO Box 156, NO-9171 Longyearbyen, Norway. (Ragnheid.Skogseth@unis.no)

2169-9275/13/10.1002/jgrc.20261

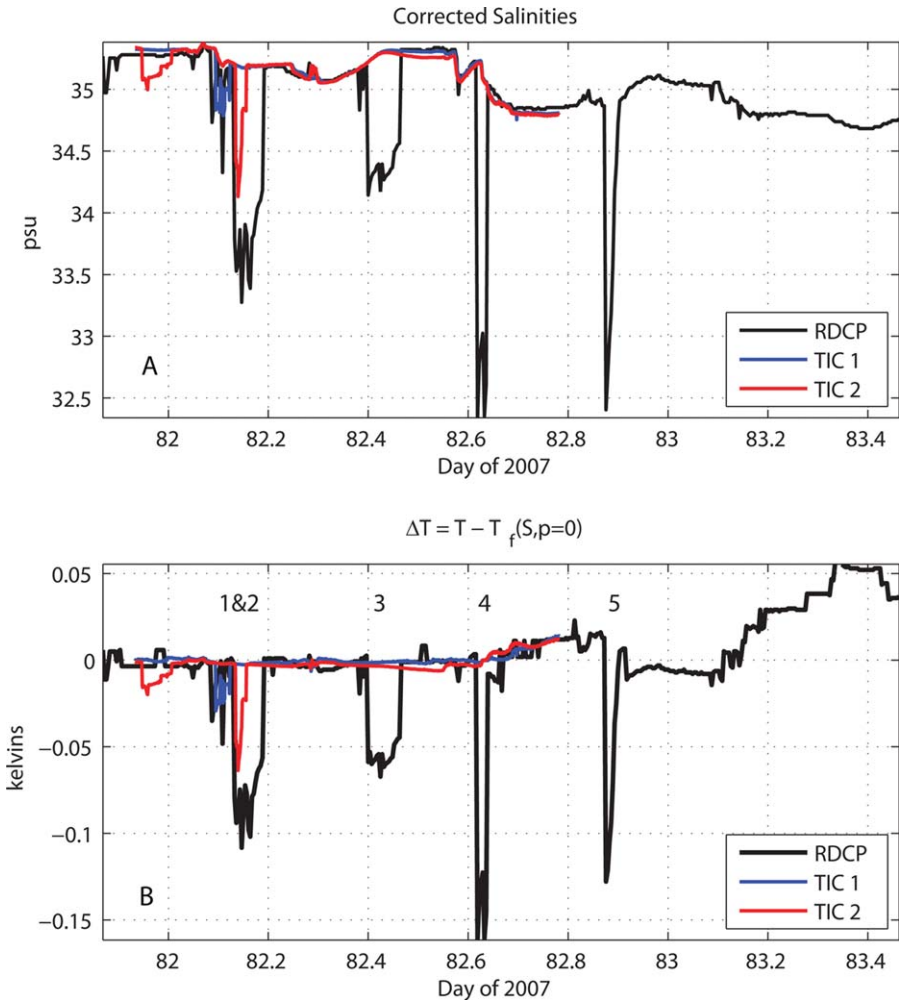

Figure 1. (a) One-minute averages of salinities measured by TIC2 (unpumped, no corrections), TIC1 (pumped), and RDCP both corrected for conductivities as described in Appendix A. (b) Departure of water temperature from freezing at surface pressure. RDCP temperature has been adjusted upward by 8 mK, with conductivity adjusted downward by 0.013 S m^{-1}. Numbers refer to "supercooling" events discussed in the text.

its in situ freezing point), apparently associated with the frontal passage. Supercooled water can form in various ways. For example, seawater in contact with cold air in leads and polynyas can become supercooled when (i) the net heat loss from the water is large and (ii) the supercooled water is transported away from existing ice before any crystallization can take place [e.g., *Coachman*, 1966]. Frazil crystals form when supercooled water encounters suitable nucleation sites, releasing latent heat and rapidly restoring water temperature toward freezing. Most commonly, frazil ice forms in regions of open water where blowing snow and other atmospheric contaminants provide plentiful nucleation opportunities. Laboratory experiments show maximum levels of supercooling of ~20–40 mK, where the supercooling level is created and varied with the heat flux and limited by the frazil ice growth [*Daly*, 1984; *Smedsrud*, 2001]. Theoretically, congelation growth of sea ice can also create supercooled water by a double-diffusive mechanism [*Mellor et al*., 1986; *Steele et al*., 1989], but a controlled study of turbulence under growing fast ice showed this effect to be of minor importance [*McPhee et al*., 2008].

[5] A different mechanism for producing supercooling is the so-called "ice pump" where water in contact with ice at depth (e.g., beneath a floating glacial shelf) is cooled to its pressure-dependent freezing point by latent exchange at the ice/water interface and then circulates adiabatically to a higher level, where its temperature is well below the in situ freezing point [e.g., *Lewis and Perkin*, 1983]. Near the Antarctic continental margins, the ice pump can produce large amounts of frazil ice [*Foldvik and Kvinge*, 1974] and platelet ice that may constitute a sizable portion of the sea ice cover near glacial shelves [*Dempsey et al*., 2010; *Robinson et al*., 2010]. It is also the likely source of extensive supercooled water found annually near the surface in McMurdo Sound, Antarctica [*Leonard et al*., 2011].

[6] Supercooling mechanisms described earlier depend in some sense on water column boundary conditions: e.g., intense heat loss to the atmosphere at the surface, or ice/ocean exchange under variable pressure conditions.

[7] Based on measurements from an ice camp on fast ice, we suggest here a novel mechanism for producing

supercooled water: one that depends directly on turbulent mixing between water masses with differing salinities, when both are near their salinity controlled freezing temperatures. The measurements were collected between 22 and 24 March 2007, at an ice camp established with support from the Norwegian Coast Guard icebreaker, K/V *Svalbard*, about 400 m into the sound from a boundary with less compact, drifting sea ice typical of Storfjorden. *Skogseth et al*. [2013] describe general conditions in Storfjorden prior to establishment of the ice camp, the instrumentation and setup of the ice camp, as well as documentation of the abrupt salinity front described earlier.

[8] This paper is organized as follows. Section 2 describes measurements and techniques, including discussion of unexpected drops in conductivity observed at different times with different instruments, and turbulent momentum and scalar exchanges near the ice/ocean boundary. Section 3 discusses the measurements in the context of an abrupt salinity (density) front advected past the instruments, including transient supercooling events. Results are summarized in section 4.

2. Measurements

2.1. Methods

[9] During the FMS ice-camp phase of the 2007 K/V *Svalbard* exercise, we deployed two turbulence instrument clusters (TICs) under fast ice about 400 m from the boundary with loosely consolidated, mobile pack ice near the entrance to the sound. Each TIC comprised a three-axis acoustic Doppler velocimeter (ADV, Sontek ADVOcean—5 MHz), with the measurement volume in the same horizontal plane as temperature and conductivity sensors manufactured by Sea-Bird Electronics. TIC1, mounted 1 m below the ice/ocean interface on a rigid rod, included a pumped temperature/conductivity pair (SBE3F/SBE4) plus a SBE7 microstructure conductivity (μC) sensor, also mounted in the same plane. TIC2 was similarly mounted 3 m below the ice/water interface but differed from TIC1 in that there was no μC component, and the standard SBE4 conductivity meter was not pumped but instead relied on the mean current to flush the small cylindrical duct housing the electrodes. The instrument was aligned with the major tidal axis to provide maximum flushing. In addition to the TICs, we obtained data from a downward oriented, Aanderaa recording Doppler current profiler (RDCP) deployed approximately 100 m away, which included temperature and conductivity from sensors in the RDCP housing suspended just below the 50 cm thick, level ice.

[10] Turbulence data from the two TICs were processed using standard procedures developed for these instruments over several previous projects [*McPhee*, 2008; *Sirevaag et al*., 2010]. Data were divided into 15 min "realizations," and deviatory values were calculated by removing a linear trend from each series, e.g., $u' = u - \langle u \rangle$ where u is the measured velocity in a direction aligned with the mean realization streamline, and $\langle u \rangle$ is a least-squares linear fit to the measured velocity over the realization period. Turbulent Reynolds stress was estimated by two methods: first by calculating the covariance of the vertical velocity with the horizontal deviatory velocity components; and second by considering the area-preserving vertical velocity variance spectra. For reasons described later we settled on calculating scalar fluxes ($\langle w'T' \rangle$ and $\langle w'S' \rangle$) by combining their variance spectra with turbulent kinetic energy (TKE) dissipation rates.

2.2. Odd Behavior of Conductivity Sensors During FMS Deployment

[11] After reconciling differences in conductivity as described in Appendix A, time series of salinity and departure of temperature from freezing (Figure 1) during the short FMS deployment reveal (i) substantial tidal changes in salinity superimposed on an overall freshening trend, and (ii) that during the first day, water temperature remained very near freezing, except for large negative excursions in conductivity lasting for tens of minutes that appeared at times on the SBE4 (standard) and Aanderaa RDCP sensors (but not on the μC instrument). These had no counterpart during the other two on-ice deployments (Van Mijenfjorden, Barents Sea) during the 2007 K/V *Svalbard* exercise, when water temperatures were generally warmer. Taken at face value they implied measurements in water supercooled to temperatures ranging from a few centikelvins to more than 0.1 K below freezing. We at first suspected one of two sources (or a combination of both) for this behavior: (i) patches of significantly supercooled water, transported from outside the fast-ice zone by the tide; or (ii) a high concentration of frazil crystals blocking the instruments, altering their conductivity. Upon further analysis, however, neither explanation appears to be entirely satisfactory.

[12] Salinity evolution during the FMS deployment is shown in Figure 2a, in which we have replaced the anomalously low-conductivity events in the RDCP record with data from TIC2 where available (or by interpolation for event 5). By removing a linear trend from the salinity record and combining the result with velocity along the major tidal axis [*Skogseth et al*., 2013], we can put the events (the shaded bars in Figure 2b) in the context of the tidal cycle. In Figure 2b, positive velocities indicate flow into FMS from Storfjorden, i.e., the flood side of the cycle. The tidal part of the salinity record appears as a rectified wave and represents advection of a relatively sharp salinity front back and forth across the instrument site. We have identified this feature with a salinity front observed offshore from the FMS fast ice in the afternoon of 23 March [*Skogseth et al*., 2013, Figures 14 and 16]. Anomalous low-conductivity events (indicated by shaded areas in Figure 2b) apparently occur (i) when current speed is near maximum and (ii) during times of rapid salinity change, i.e., frontal passage. In the RDCP record they occur on both the flood and ebb phases. Their absence on day 83 (24 March) is not surprising, as the water warmed to above freezing (Figure 1b).

[13] We examined the anomalous events in more detail by considering the response of the SBE4 conductivity meters in the first few hours of 23 March (Figure 3). Temperatures measured at TIC1 (1 m from ice) and TIC2 (3 m) agree to within about a millikelvin (mK) and showed a rapid, albeit small rise beginning about 02:15 (UT) at about the same time that salinity began to decrease at all TIC sensors, marking the arrival of fresher water from outside the fast-ice zone. Salinity time series are shown in Figure 3b

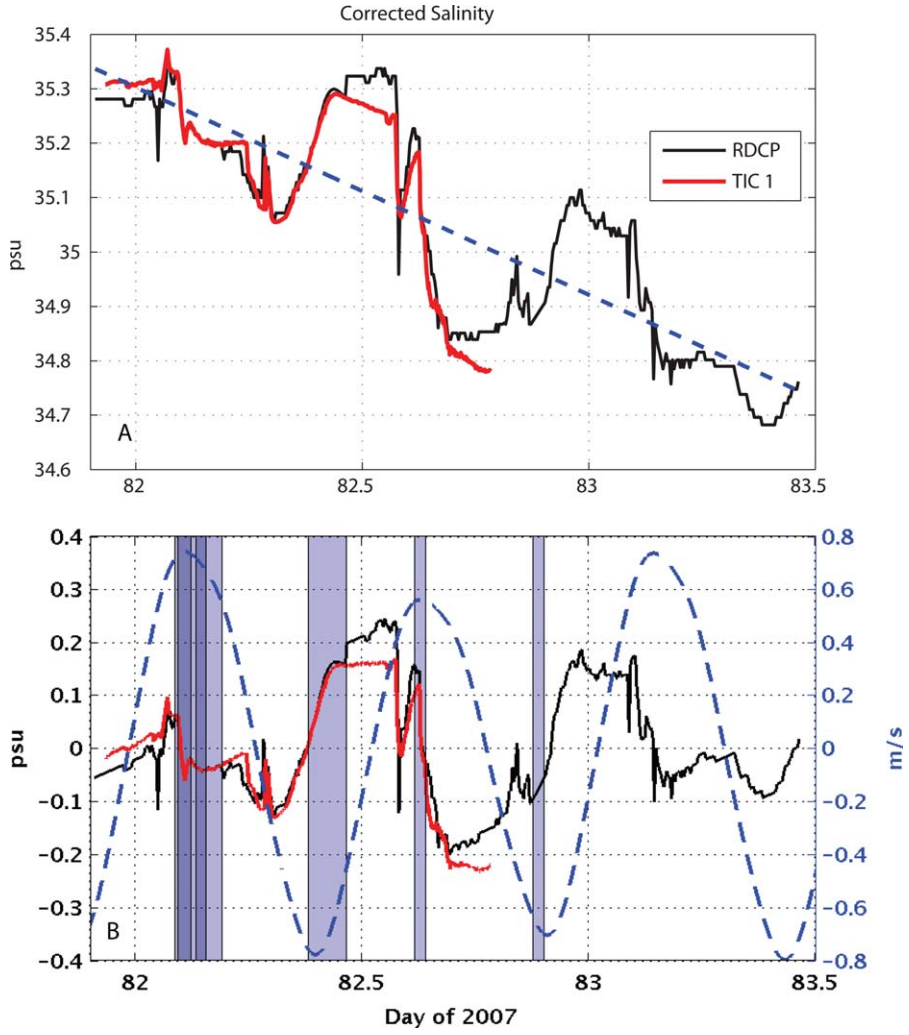

Figure 2. (a) Corrected salinity from the RDCP (black) and TIC1 (red), with linear trend indicated by the dashed line. (b) Salinity anomaly plotted together with barotropic tidal velocity along the major tidal axis (positive into FMS). Light shading indicates times of conductivity drops in the RDCP record. Heavier shading indicates drops in the TIC standard C records, corresponding to events 1 and 2 as identified in Figure 3b.

from three instruments with calibration adjustments as explained in Appendix A: the pumped SBE4 instrument on TIC1 (C_1, blue); the SBE7 microstructure conductivity instrument on TIC1 (μC, red), and the standard (not pumped) SBE4 instrument on TIC2 (C_2, green), 2 m lower. Events 1 and 2, and a similar dropout in RDCP conductivity (Figure 1), all occur within an hour and a half after flood maximum, during a time of intense mixing. Event 1, sensed by the C_1 sensor (pumped), lasted for about 40 min, and then reverted to values near those sensed by the other two instruments. About 15 min later, event 2 occurs in the other standard SBE4 instrument, 2 m lower, and lasts for about half an hour. Significantly, neither event is evident in the μC salinity.

[14] These observations are difficult to reconcile with the possible sources identified earlier. If, for example, a mass of water supercooled to 50 mK had indeed advected under the fast ice from outside the sound, it is difficult to see how it would appear at the upper TIC almost an hour before the lower. Both events occurred during a time of high currents and vigorous turbulent mixing. Because of boundary-induced shear from the fast-ice cover, we expect water with lower salinity to appear first at the lower site, as discussed later. Given the levels of turbulence in the flow, it also seems quite unlikely that separate, low-aspect lenses of supercooled water at different depths in the upper 3 m could persist long enough after encountering the fast-ice boundary to produce the observed events.

[15] It is perhaps less easy to dismiss the idea that advection of frazil ice crystals from elsewhere could account for the events; however, several factors argue against this interpretation. Whereas it is plausible that during the flood tide, frazil crystals generated by air-sea fluxes in low concentration pack in Storfjorden proper could be swept past our instrument sites and in fact might sustain a vertical gradient that would cause them to appear first at the shallower site, it is difficult to imagine a source well within the limits of the solid fast ice that would produce similar behavior on

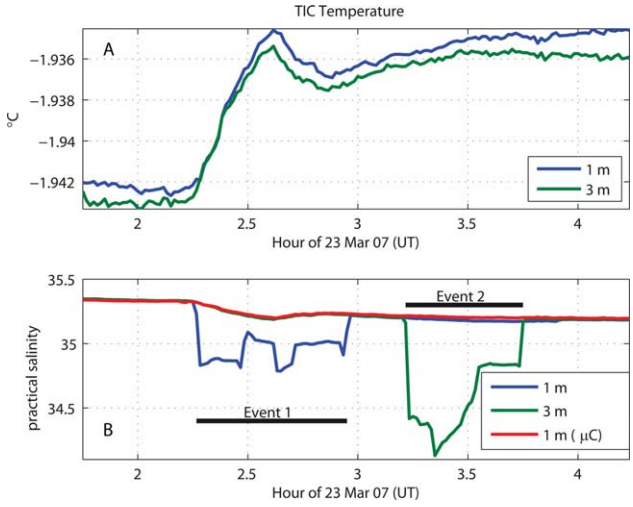

Figure 3. (a) TIC temperatures measured during dropout events early on day 82. (b) Adjusted salinity at TIC1 (pumped, blue; μC, red) and TIC2 (green).

the ebb tide. There are instrumental considerations as well. Typically, with SBE4 instruments, it is readily apparent when ice blockage occurs, because conductivity drops to values near zero. Here the inferred salinity values remain within somewhat plausible ranges. The μC instrument, mounted quite close to the intake of the pumped T/C pair on TIC1, did not indicate lower conductivity during event 1 and showed little evidence of crystals striking or passing between the small exposed dual electrodes. We also examined the echo intensity of the Sontek ADVOcean acoustic backscatter velocimeters (Figure 4). We would expect a cloud of frazil crystals appearing for 20 min at TIC1 (event 1) and later for 15 min at TIC2 to induce quite different echo amplitudes from the respective velocimeters, but the differences are minimal. Even in the 1 min average time series, they are often highly correlated, which would be expected from "normal" turbulence during both events.

[16] There is reasonably convincing evidence that the low-conductivity events are indeed linked to supercooling, even if the magnitudes seem far too large. Using our best estimates for temperature and salinity at levels 1 and 3 m below the ice undersurface, the departure of water temperature from freezing at surface pressure (ΔT_0) indicates (Figure 5a) slight (1–2 mK) supercooling at both levels. Two factors need to be considered in discussing this result: first, the magnitude of ΔT_0 is comparable to the uncertainty in SBE3 thermometer calibration; and second, it is smaller than the uncertainty cited by *Gill* [1982] in the United Nations Educational, Scientific and Cultural Organization, Paris (UNESCO) freezing temperature formula, which we have used here and is given by

$$T_f(S,p) = -0.0575S + 1.710523 \times 10^{-3} S^{3/2} - 2.154996 \times 10^{-4} S^2 - 7.53 \times 10^{-3} p$$

where S is the salinity on the practical salinity scale and p is the pressure in bars (10^5 Pa). Despite these uncertainties, it is clear that ΔT_0 decreases in the first half hour, with a slightly lower value at 3 m. When the small pressure correction in the UNESCO formula is applied (Figure 5b), ΔT_p begins positive at both levels, but the positions are reversed, with minimum ΔT_p at TIC1 (1.5 dbar) coinciding closely with event 1, and similarly, event 2 begins near the time that TIC2 (3.5 dbar) ΔT_p decreases to within about 0.5 mK of freezing. Consequently, it seems reasonable to infer that the time lag between events 1 and 2 is related to the pressure dependence of freezing temperature. Starting at about 02:15, water temperature increase (Figure 3a) coincides with the arrival of fresher water (still near freezing) from offshore of the fast ice. Note that during the period of rapid temperature rise lasting for about the next half hour ΔT_p continues to decrease at TIC2 until it reaches a value very close to freezing.

[17] These observations suggest that the dropouts observed in both the standard SBE4 conductivity meters occurred as the water reached a transient supercooled state and nucleated on the small glass ducts housing their resistance-measuring electrodes, in effect decreasing their diameter and increasing apparent resistivity. We think similar nucleation on the electrode surface of Aanderaa RDCP conductivity sensor accounts for its sudden drops in conductivity, and that events 1–5 are in fact localized, transient supercooling episodes.

2.3. Stress, TKE Production, and Dissipation

[18] Three-axis Sontek ADVOcean current data provided estimates of turbulent stress along with TKE production and dissipation as follows. Friction speed (square root of the local kinematic turbulent stress) was calculated directly from the covariance of the deviatory velocity components using 1 h bin averages of the 15 min turbulence realizations:

$$u_* = (\langle u'w'^2 \rangle + \langle v'w'^2 \rangle)^{1/4} \quad (1)$$

[19] We also calculated area-preserving vertical velocity variance spectra following the procedure described by *McPhee* [1994, 2008], which provides estimates of two important turbulence parameters: (i) the dominant turbulence scale (mixing length), $\lambda = c_\lambda / k_{max}$, where k_{max} is the angular wave number at the peak of the area-preserving (weighted) vertical velocity variance spectrum [$kS_{ww}(k)$] and $c_\lambda \approx 0.85$; and (ii) the dissipation rate, estimated from the

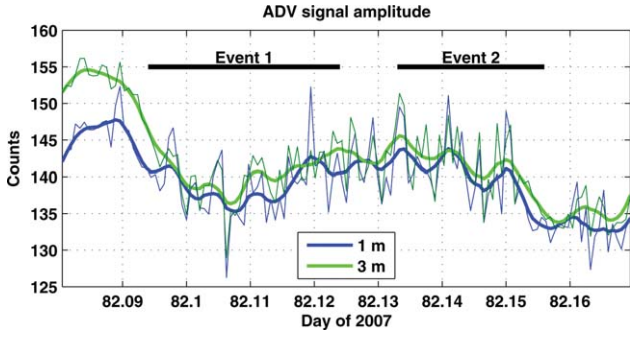

Figure 4. ADV echo amplitude during the two dropout events in TIC conductivity. Light traces are the 1 min average amplitude of three beams for each ADVOcean instrument. Heavy traces are 5 min running average.

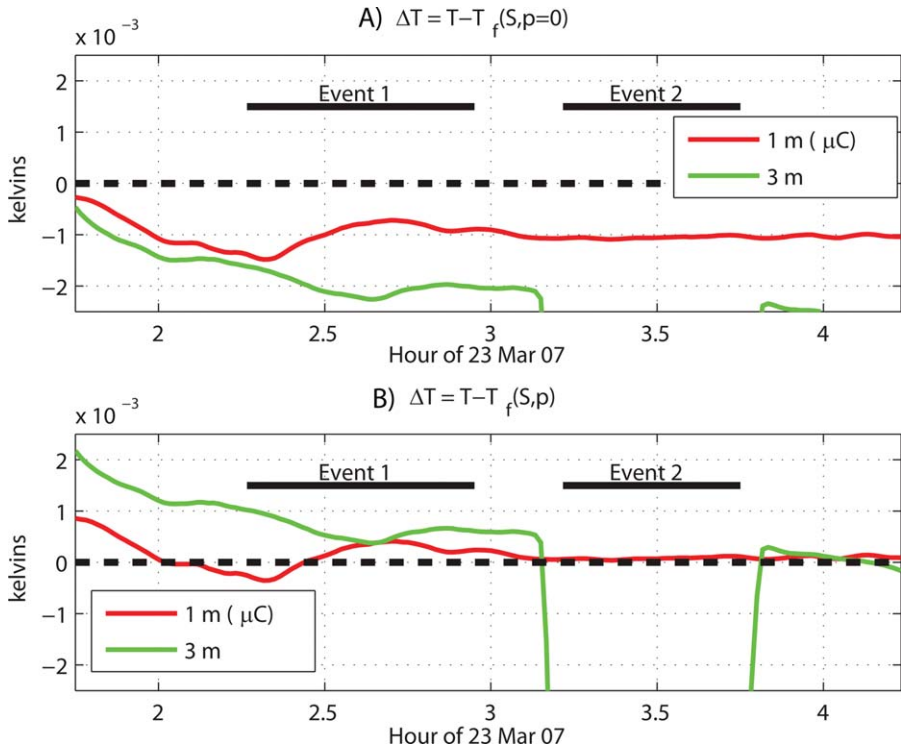

Figure 5. (a) ΔT calculated at surface pressure ($p = 0$) for salinities from TIC1 μC (red) and TIC2 standard C (green). (b) ΔT corrected for pressure (1.5 dbar for TIC1, 3.5 dbar for TIC2).

spectral level at a wave number, k_ε, in the $-2/3$ (inertial) subrange of the area-preserving log-log vertical velocity (w) spectrum

$$\varepsilon = \frac{3}{4\alpha_\varepsilon} S_{ww}(k) k_\varepsilon^{5/3} \tag{2}$$

where $\alpha_\varepsilon = 0.51$ is the Kolmogorov constant for the along-stream spectrum.

[20] If local stress and shear are related by local eddy viscosity, $u_*\lambda$, TKE shear production is estimated as $\tau \frac{\partial u}{\partial z} = \frac{u_*^3}{\lambda}$. In a turbulent regime where the TKE shear production is approximately balanced by dissipation, the vertical velocity spectrum then by itself provides an independent estimate of friction velocity

$$u_{*(\varepsilon)} \approx (\lambda\varepsilon)^{1/3} \tag{3}$$

[21] Conversely, by using the covariance estimate of friction speed, TKE production may be estimated instead by $P_S = u_{*(cov)}^{1/3}/\lambda$.

[22] Maximum values of about 0.8 m s^{-1} during both flood and ebb are shown from hourly averages of current speed (Figure 6) at 3 m. As expected, there is significant shear between the two clusters. The two estimates of friction speed (covariance, spectral) are reasonably similar overall (Figures 6b and 6c), although there are periods of significant difference, the largest of which occurs during the ebb tide. Then $u_{*(\varepsilon)}$ values for both clusters are smaller than during the two flood events, while this holds only for TIC2 in the $u_{*(cov)}$ time series. The master turbulence scale inferred from the spectral peaks (Figure 7a) often approaches the geometric scale ($\kappa|z|$, where κ is Kàrmàn's constant) for TIC1 but is consistently smaller for the 3 m cluster, indicating that other factors in the flow influenced turbulence scales fairly close to the interface. TKE production (Figure 7b; based on the covariance estimate of u_*) accentuates the asymmetry between flood and ebb, particularly at the 3 m level. TKE dissipation, based on w spectral levels, also illustrates this marked asymmetry. At the 1 m level during flood episodes, dissipation exceeds production, which suggests a source of turbulence in addition to local shear. The opposite holds during the ebb tide. At 3 m, this pattern is not so clear, although overall dissipation slightly exceeds production.

[23] Assuming that the 1 m level satisfies surface-layer criteria (as indicated by the correspondence between λ and $\kappa|z|$), hydraulic roughness is obtained from the "law of the wall":

$$\log z_0 = -\frac{\kappa u}{u_{*0}} + \log(1) \tag{4}$$

[24] Average values for $\log z_0$ are -10.7 and -11.4 using $u_{*(cov)}$ and $u_{*(\varepsilon)}$, respectively, with corresponding z_0 values: 2.2×10^{-5} and 1.1×10^{-5} m. These are very small, but not widely different from hydraulic roughnesses observed under fast ice elsewhere [e.g., *Crawford et al.*, 1999; *McPhee et al.*, 2008].

2.4. Scalar Fluxes

[25] Estimating turbulent heat flux $\left(H_f = \rho c_p \langle w'T' \rangle\right)$, where ρ is water density and c_p is specific heat

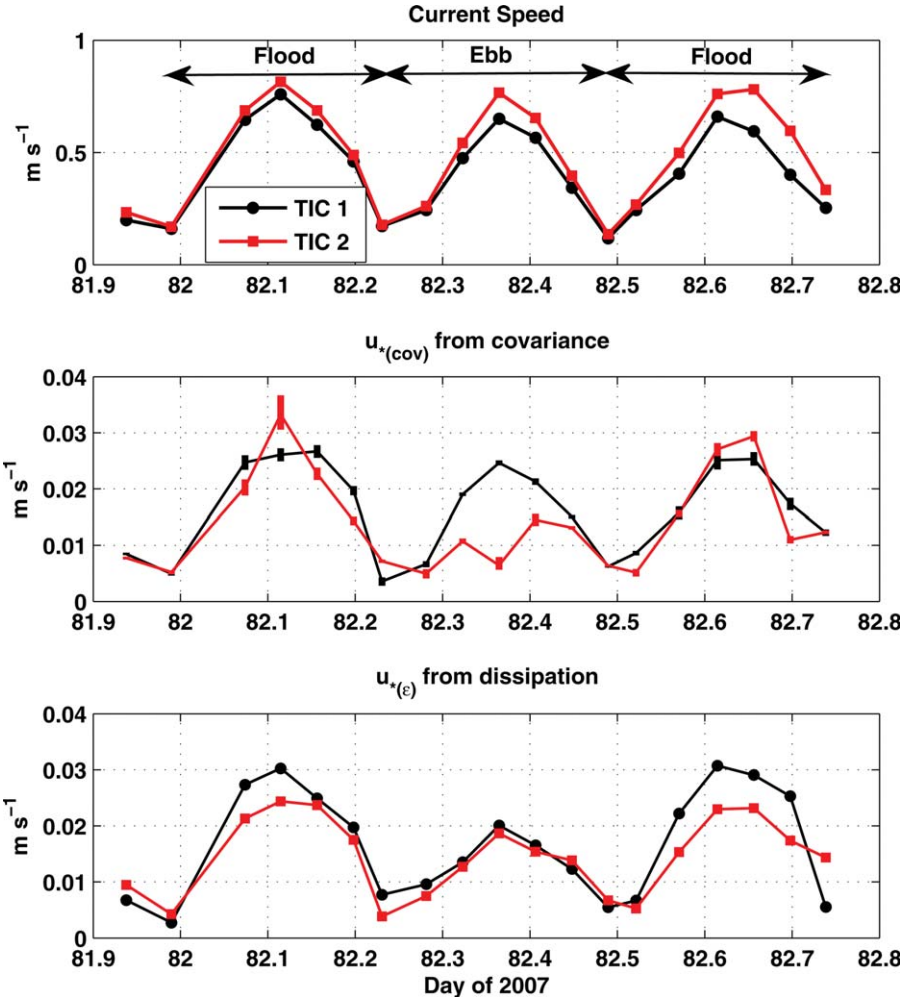

Figure 6. (a) Hourly average current speed 1 m (TIC1, circles) and 3 m (TIC2, red squares) below the ice. Bars represent ±1 standard deviation from the mean. (b) Friction velocity from Reynolds stress estimated from covariance statistics. Bars represent confidence limits for the hourly average covariance estimates. (c) Friction velocity estimated from dissipation and mixing length, both obtained from vertical velocity spectra.

(approximately 4.1×10^3 J kg^{-1} for cold seawater) during the FMS deployment presented a difficult challenge because (i) deviations in temperature were often very small despite the intense turbulence, and (ii) when changes in temperature occurred (e.g., Figure 3a), they were associated with the passage of the advected front. These were often very abrupt, as illustrated by the arrival at the turbulence mast of relatively cold, more saline water with the ebb (outward) tide in the morning of 23 March (Figure 8a), and the later arrival of fresher, warmer water with the afternoon flood tide (Figure 8b) as the front separating the two water types advected back into the sound. In each case, the change in "mean" temperature between minutes 9 and 12 is larger than the turbulent fluctuations yet occurs at a comparable time scale. Such events were not uncommon during the frontal passages, which often included smaller-scale structure embedded in the front (e.g., Figure 2). In these circumstances, covariance statistics are sensitive to removal of the "mean" flow. Using the example for TIC2 in Figure 8b, the covariance calculated by our standard method of removing a linear trend over the 15 min segment is $\rho c_p \overline{w' T'}_{linear} = -42$ W m^{-2}, whereas if we instead remove a quadratic fit (allowing more realistic curvature), the result is -8 W m^{-2}, a fivefold difference. For comparison if we use the same procedure for comparing friction velocity during the same data segment, the difference between removing a linear fit of the horizontal velocity components versus a quadratic fit is minimal: $u_{*(linear)} = 0.030$ m s^{-1}; $u_{*(quad)} = 0.029$ m s^{-1}. The reason, of course, is that there is no abrupt change in momentum of the flow comparable to the change in temperature.

[26] Since direct covariance estimates of heat flux seemed questionable, we instead considered spectral estimates of heat flux magnitude, obtained from a combination of thermal variance dissipation from spectral density in the inertial subrange [e.g., *McPhee*, 1994, 2008]

$$\varepsilon_T = \frac{S_{TT} \varepsilon^{1/3} k^{5/3}}{\alpha_\theta} \tag{5}$$

[27] ($\alpha_\theta = 0.81$ is the thermal Kolmogorov constant), and the conservation equation for thermal variance

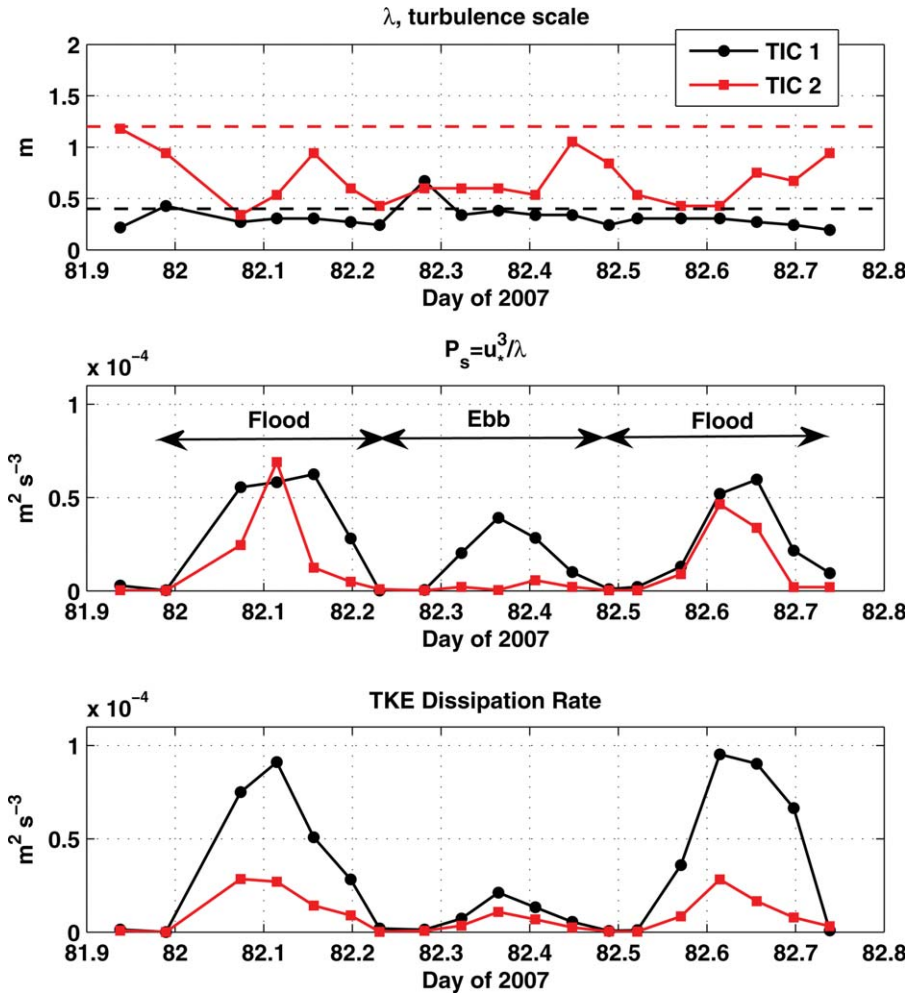

Figure 7. (a) Mixing length λ inversely proportional to the wave number at the peak in the area-preserving w spectrum. Dashed lines indicate the geometric scale $\kappa|z|$. (b) Shear production rate of TKE from the covariance estimates of u_*. (c) Dissipation estimated from spectral density in the inertial subrange of the w spectrum.

$$\left|\langle w'T'\rangle \frac{\partial T}{\partial z}\right| = \frac{k_{max}\langle w'T'\rangle^2}{c_\lambda u_*} = \varepsilon_T \tag{6}$$

[28] Our reasoning in choosing the spectral method is that in a rapidly moving, heterogeneous flow (i.e., with significant horizontal gradients in mean quantities) turbulence characteristics in the inertial subrange would be more representative of the actual flux magnitudes. We made the following assumptions to extract heat flux magnitude from (5) and (6): first, that eddy heat diffusivity is nearly the same as eddy viscosity (i.e., $K_H \approx K_m = u_*\lambda$), and second that the wave number, k_ε, used to evaluate TKE dissipation from (2) is the same for thermal dissipation. To specify heat flux direction, we considered the sign of the difference between temperatures measured at 1 and 3 m. Since these differences were often very small, we adjusted T_1 so that it agreed with T_2 during times of small heat flux magnitude. Results (Figure 9) indicate relatively small vertical heat flux except at 3 m during the second flood event, which coincides with a rapid rise in temperature beginning shortly after 82.6. A possible explanation for higher temperatures and larger heat flux in the second flood is slight heating from solar insolation in lower concentration ice offshore from the fast-ice edge (local solar zenith was at approximately 10:45 UT). Despite this warming and large friction velocity, the water remained near enough freezing that basal heat flux calculated according to a bulk formulation for sea ice: $H_{bulk} = \rho c_p c_H u_{*0}\left[T_{ml} - T_f(S_{ml})\right]$ with $c_H = 0.0057$ [*McPhee et al.*, 2008] never exceeded 3.2 W m^{-2}. For the bulk relation we calculated u_{*0} from current speed at 1 m using (4).

[29] As indicated earlier, problems with the pumped TIC1 conductivity meter precluded using its record for covariance estimates of salinity flux, and even after accounting for its lag in response; we noticed at times fairly large deviation from the other sensors during the FMS deployment. These differences were not present during the other two deployments. Having used the low-pass filtered TIC2 conductivity to establish a time-dependent intercept for the linear μC calibration (see Appendix A), we were unable to determine small differences in salinity at the two levels. The rapidly changing frontal structure apparent in

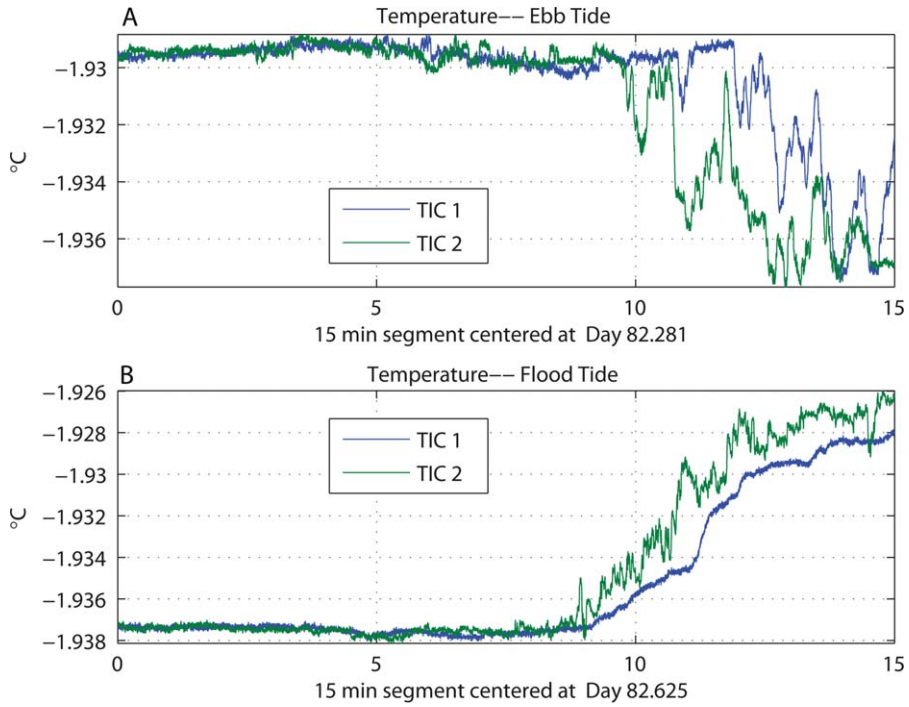

Figure 8. Temperature measurements at 1 and 3 m below the ice for 15 min data segments during (a) ebb and (b) flood events on 23 March 2007. In each, a small correction to T_1 (<1 mK) has been added so that mean temperatures in the first 8 min coincide.

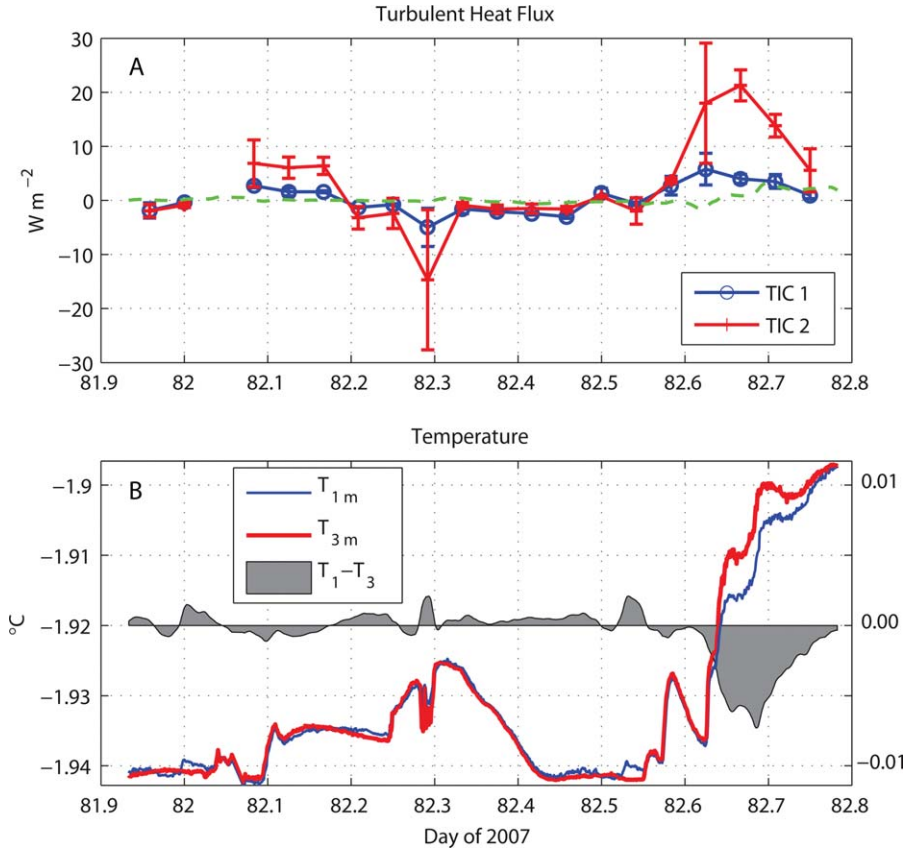

Figure 9. (a) Hourly average heat flux estimates from spectral characteristics at 1 m (blue) and 3 m (red). Error bars represent ±1 standard deviation of the spectral magnitude estimates. The green trace indicates interface (basal) heat flux based from bulk parameterization. (b) Temperatures at the two TIC levels (left scale), with the 1 m thermometer adjusted downward by 1.3 mK, determined at times when the heat flux magnitude was small. Shaded area indicates the temperature difference in kelvins (right scale).

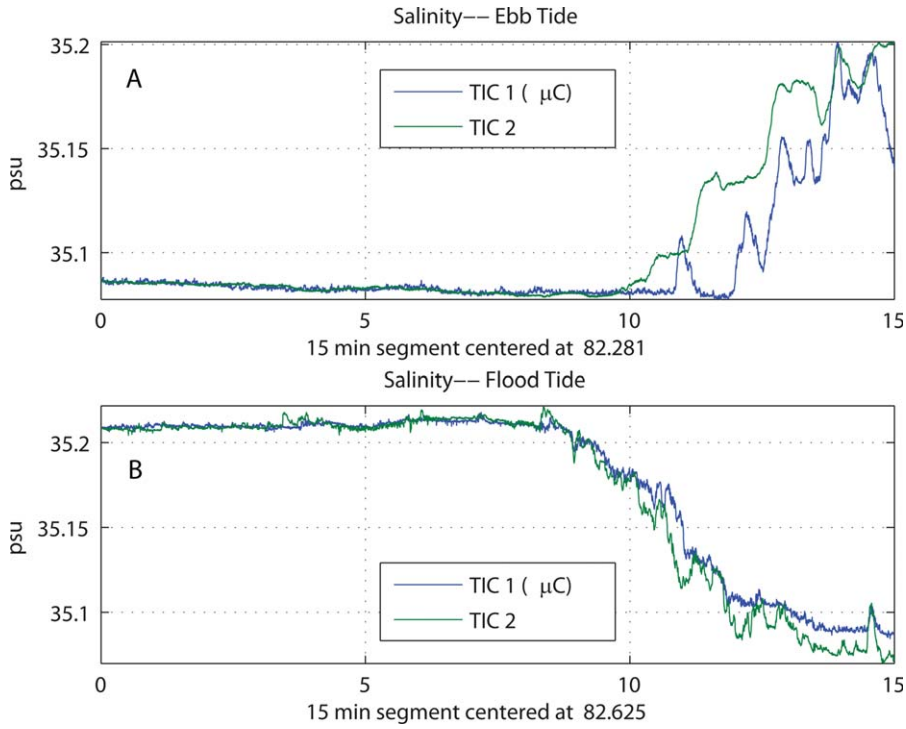

Figure 10. Same as Figure 8, except for salinity, with μC salinity adjusted so that mean values agree in the first 8 min of both records.

temperature was even more pronounced in salinity (Figure 10), so we also utilized the spectral method for estimating salinity flux, i.e., the haline equivalents of (5) and (6), assuming that the thermal Kolmogorov constant was suitable for salinity. As suggested by Figures 8 and 10, we assigned direction based on the negative of the thermal gradient, which combined with the spectral magnitude estimates, provided a time series of salinity flux at the two levels (Figure 11). Two factors argue against considering results of Figure 11 as quantitatively correct. First, in addition to the assumptions implicit in the thermal spectral flux magnitude calculation, the standard TIC2 conductivity meter depends on mean flow for flushing (its duct was oriented along the major tidal axis); hence, the impact of time lag between the conductivity sensor and thermometer is not well known (which affects salinity), perhaps exacerbating the horizontal homogeneity problem mentioned earlier. Second, as discussed later, there is reason to believe that eddy diffusivities for heat and salt differ, implying different scalar Kolmogorov constants. Nevertheless, estimates from the two different sensors are qualitatively consistent and suggest fairly strong downward salinity flux during the flood events and a weaker upward flux during the ebb. At these low temperatures, buoyancy is controlled almost exclusively by salinity. The downward salinity maximum at time 82.667 corresponds to a destabilizing buoyancy flux of about 2×10^{-7} m^2 s^{-3}.

3. Discussion

3.1. Turbulence in a Moving Horizontal Density Gradient Near a Solid Boundary

[30] *Crawford et al*. [1999] showed that when a horizontal gradient in density advects under a fast-ice boundary, current shear near the interface induces substantial changes to the turbulent flow structure, in a manner similar to estuarine tidal straining as described by *Rippeth et al*. [2001]. Results described earlier illustrate the importance of this process in FMS, even relatively close to the boundary in a highly turbulent environment. Consider first the short *T* and *S* time series in Figures 8 and 10. On the ebb tide (Figures 8a and 10a), the front is exiting the sound, and interior (saltier, colder) water appears first at the lower cluster on the TIC mast. At low temperature, density is controlled almost exclusively by salinity, so when the front is outbound, the effect is to vertically stabilize the water column. During the flood (lower panels), positions are reversed, with slightly fresher, warmer water from outside the fast-ice zone underrunning the colder, saltier water mass of the

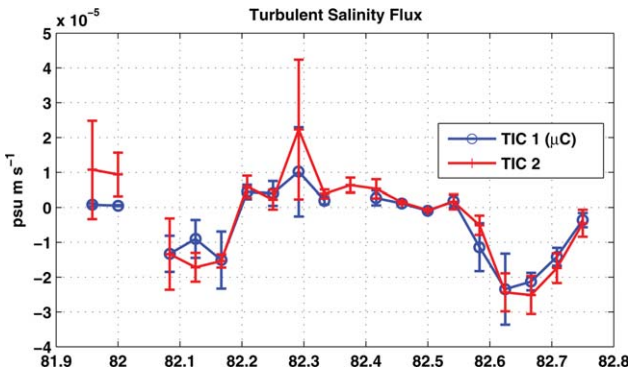

Figure 11. Hourly average salinity flux estimates from spectral characteristics at 1 m (blue) and 3 m (red). Error bars represent ±1 standard deviation of the spectral magnitude estimates.

inner sound. The impact then is to create a statically unstable water column, gravitationally enhancing the shear-generated turbulence. This qualitative description of the impact on turbulence of the horizontal density gradient is borne out by the measurements presented in Figures 6 and 7. In the former, current speeds during flood (centered around times 82.1 and 82.65) are similar to the ebb, but there is a marked reduction in friction velocity, especially at the lower level, 3 m from the interface. At TIC1 (1 m below the interface) this flood/ebb asymmetry also carries over to the TKE shear production (P_S) and dissipation ε (Figure 7). During flood events both P_S and ε are larger than ebb values. Furthermore, during flood events dissipation exceeds shear production, suggesting a positive TKE buoyancy source (i.e., $P_b = \langle -w'b' \rangle$), whereas during the ebb event, $P_S > \varepsilon$, which would be expected with a negative buoyancy source (sink). At TIC2, shear production and dissipation appear to be more closely balanced.

[31] These observations are consistent with the echo amplitude data from the RDCP [Figure 13b in *Skogseth et al.*, 2013]. Assuming echo amplitude reflects in some way turbulent intensity in the water column, the higher amplitudes penetrate much farther down in the water column on the flood (freshening, statically unstable) than on the ebb (increasing salinity, statically stable).

[32] As described in section 2.4, the accuracy of our scalar flux estimates ($\langle w'T' \rangle$ and $\langle w'S' \rangle$) is highly questionable because during the frontal passages, mean values of temperature and salinity change rapidly on time scales comparable to the time scale of the energy containing eddies. Generally, a condition for invoking conservation of scalar variance (6) to estimate fluxes is horizontal homogeneity, which is clearly violated here. Still, the qualitative sense of the estimates is consistent with shear-induced mixing as described earlier: during the two flood events salt is mixed downward as fresher water underruns saltier, and heat is mixed upward because the introduced fresher water, being near freezing, is slightly warmer than the water above, which is also near freezing. In the single ebb event during which fluxes were estimated, the opposite holds.

3.2. Conductivity Measurements in Supercooled Seawater

[33] Given the premise that the low-conductivity events indicate nucleation on the instrument electrode surfaces and thus signal the presence of supercooling, Figures 1 and 2 show that nucleation occurred on the RDCP sensor in four different episodes encompassing both flood and ebb of two tidal cycles, whereas it appeared on the two SBE4 standard conductivity sensors only during the first flood cycle, early on day 82. The SBE7 microstructure instrument never exhibited a sustained dropout in the same way. A possible explanation for this difference among the sensors might be variations in surface curvature of the electrodes: the flatter the surface, the less resistance to developing an ice coating. Mixing intensity might also play a role: the TICs were deployed under very smooth ice, while the RDCP was closer to highly deformed areas.

[34] Subsequent to the 2007 Storfjorden project, one of us (M.G.M.) had an opportunity to again deploy TICs in a supercooled seawater environment, near Erebus Glacier Tongue, Antarctica, in collaboration with New Zealand scientists (NIWA project K132). In late October 2010, we deployed a mast identical to the FMS mast about 140 m from the glacier tongue with TICs 1 and 3 m below the ice, along with a second mast nearer the tongue that could be lowered to depths exceeding 60 m. The water column was close to isothermal in the upper 60 m, reaching its pressure-dependent freezing temperature at a depth of about 15 m, above which the water was supercooled. This was confirmed by platelet ice growth to that level on the cable suspending the second mast. After a few days, nucleation of ice on the mast 1 (shallow) ADVs degraded performance enough to warrant its recovery; however, during the deployment period one of the SBE4 conductivity meters (not pumped) exhibited behavior somewhat reminiscent of the experience at FMS (Figure 12). Conductivity at 3 m decreased by steps, apparently related to the dominant diurnal tidal cycle at Erebus Glacier Tongue. By DOY 303 (30 October 2010), its conductivity indicated salinity about 0.2 psu less than 2 m higher, which is physically untenable. None of the other conductivity sensors at the station showed a similar drop: e.g., a TIC stationed at 40 m depth for about 3 days, approximately 100 m away (+ symbols), is slightly greater than at 1 m, consistent with a small salinity gradient observed in the upper 50 m. As before, we attribute the drop in conductivity of the 3 m instrument to slow accretion of a layer of ice on the duct housing the SBE4 electrodes, slowly reducing its diameter and increasing measured resistivity. Unlike FMS, there was no source of above freezing water to remove the ice layer. It might be appropriate to point out that, had the 3 m conductivity cell been our only source of salinity data, a reasonable but false inference would have been that each tidal cycle brought slightly fresher water into the local region.

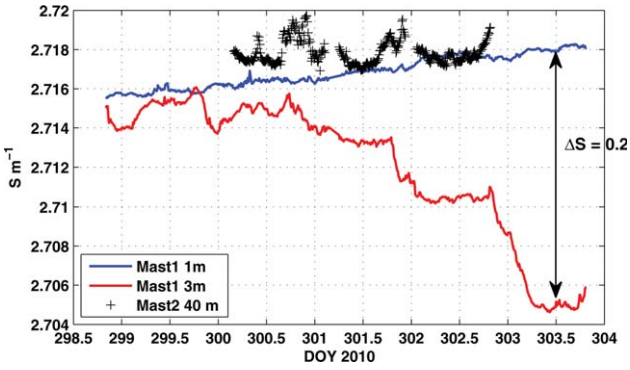

Figure 12. Conductivity measured in late winter in McMurdo Sound near Erebus Glacier Tongue. Mast 1 conductivity meters (1 and 3 m below the ice/water interface) were in supercooled water. The Mast 2 TIC was at 40 m, in water about 20 mK above its in situ freezing temperature. The arrow shows the difference in salinity (practical salinity scale) indicated by the conductivity difference at the end of the period. The conductivity meter at 1 m was pumped; the meter at 3 m was not.

3.3. Supercooling by Mixing: Double-Diffusion Hypothesis

[35] The low-conductivity events occurred (Figure 2) near peak tidal flow when a sharp front in salinity passed our measurement site as it rode the tide in and out of the

entrance to FMS. Given our interpretation of the events as signaling the presence of supercooled water (but not its true magnitude), it thus appears that zones of local supercooling were embedded within the front. In what follows we examine the hypothesis that this supercooling resulted mainly from vertical mixing of heat and salt characteristics of the two different water masses separated by the front, and that the supercooling occurred because heat was transferred locally faster than salt. In other words, we are suggesting a process by which supercooling occurs by double-diffusive mixing processes within the water column, and not from direct surface or boundary heat and salt transfer.

[36] The hypothesized process involves two elements: first that the frontal passage induced significant vertical gradients in T and S, and consequent turbulent mixing; and second, that double-diffusive mixing caused localized supercooling in the water masses that were separately very close to their salinity controlled freezing temperatures. The former is a fairly straightforward consequence of vertical shear near the fast-ice boundary acting upon the horizontal gradients, as demonstrated earlier. The latter is less obvious, and in fact requires some violation of Reynolds analogy, i.e., that eddy viscosity and scalar eddy diffusivities are all about equal in highly turbulent flow. If turbulent diffusivities are the same for all scalars (Reynolds analogy), then combining two water masses with different salinities, each at its in situ freezing temperature, would result in a mixture still at its freezing temperature (departure from freezing due to the miniscule curvature in the UNESCO freezing formula was found to be negligibly small), i.e., there would be no supercooling. However, in the mixing process, if thermal eddy diffusivity exceeds haline eddy diffusivity, then heat would transfer from the fresher, warmer water type to the saltier, colder water faster than salt moved in the opposite direction, in effect supercooling the fresher constituent. Note that this process could occur regardless of the flow direction; only the mixing intensity would change depending on the direction of the salinity flux.

[37] We considered an alternative hypothesis, based on the "heat pump" concept. Suppose that at slack tide the water column was isothermal at its surface-pressure freezing temperature, and that a layer of frazil crystals had collected near the ice/water interface. As the tide strengthened, turbulent eddies generated by shear would mix the frazil downward. At depth, the frazil would encounter water above its in situ freezing temperature and melt, thereby producing water that would appear supercooled as it was mixed back toward the surface, accounting for the transient events observed at shallow depths during the flood and ebb tides. In this view, supercooling near the surface would result from large-scale vertical mixing, rather than mixing associated with sheared horizontal temperature and salinity gradients during frontal passage. Their only impact would be in changing the turbulent forcing as described in section 2.2. Our data posit several objections to this scenario. First, there is little evidence in either the conductivity or ADV records of frazil either collecting or passing through levels 1 and 3 m below the interface, during the supercooling events. Second, the vertical turbulence scales inferred from flow statistics (Figure 7a) do not suggest deeply penetrating eddies. They are an order of magnitude smaller than scales associated with convection measured at the edge of a freezing lead [*McPhee and Stanton*, 1996]. Third, the only plausible source for replenishing melted frazil would be advection from outside (flood), yet the supercooling appears on both the flood and ebb cycles. Finally, a conductivity-temperature-depth (CTD) station taken at the edge of the fast ice near slack tide, in the water mass representative of the interior sound [*Skogseth et al*., 2013, Figure 18], shows no evidence of water with temperature below the surface-pressure freezing point, a requirement for the heat pump mechanism.

4. Summary

[38] Despite its short duration, our measurement program near the edge of fast ice in FMS provided a fascinating look at processes that occurred when a relatively narrow front separating water masses with different salinities and temperatures near freezing encountered a fixed upper boundary as it rode on a strong tidal current. Turbulence measurements near the ice/water boundary confirmed that vertical shear of the horizontal density gradient had significant impact on stress and TKE production and dissipation (section 2.3). These results were confirmed by turbulent flux of scalar quantities, at least qualitatively (section 2.3).

[39] The FMS measurements also provided an opportunity to observe concurrently the performance of multiple conductivity meters when conditions hovered near the in situ freezing temperature. Our preferred explanation for sudden drops in conductivity observed at different times on the various instruments is that when the sensors encountered supercooled water, ice accreted on surfaces housing the electrodes, increasing apparent resistivity. In our interpretation, small modifications to sensor geometry induced changes to resistivity that implied transient events of large, but not wholly unrealistic supercooling (Figure 1b). Considered in isolation without the context provided by other nearby measurements, it would have been natural to accept these at face value. This suggests caution in interpreting conductivity data from an isolated instrument in water that may be potentially supercooled.

[40] Despite the rather strange response of our conductivity measuring instruments during passage of the salinity front, we believe they indicated transient supercooling events, and that double diffusion provides a plausible mechanism for their occurrence. A drawback to this explanation for the supercooling events is that it directly challenges strict application of Reynolds analogy for scalar and momentum transfer in a flow with very high turbulent Reynolds number [e.g., *Hinze*, 1975]. There are, of course, well-known examples of double diffusion in the ocean, but most are associated with low turbulence levels. An exception is an event reported by *McPhee et al*. [2005], who showed that heat had been extracted from the upper pycnocline faster than salt, when an upwelling episode apparently forced by Ekman pumping during horizontal ice shear, encountered a highly turbulent boundary layer. These results are not inconsistent with a laboratory study reported by *Krylov and Zatzepin* [1992], who found evidence of double diffusion at relatively high turbulence levels in a

stirred, salt-stratified tank and suggested that it was important in frazil ice production.

[41] If our hypothesis for how supercooling can result from mixing at a boundary between cold water masses with differing salinities withstands further observational scrutiny, it suggests a novel mechanism that depends only on mixing within the water column and requires neither surface heat and salt exchange as in latent heat polynyas [*Skogseth et al*., 2008], nor large changes in pressure as encountered in ice shelf cavities.

Appendix A: Adjustments to *T* and *S* Time Series

[42] The combination of two TICs plus the nearby RDCP sensors provided three independent temperature time series and four separate conductivity records (Figure A1), all taken relatively near the ice-ocean interface. In general, the TIC (Sea-Bird Electronics SBE3) temperatures agreed well (within 1–2 mK). Both have higher resolution and read somewhat warmer than the RDCP temperature (Figure A1a). We reconciled the RDCP temperature with the SBE sensors by applying a constant correction of 0.008°C.

[43] Time series of conductivity from the standard SBE4 and RDCP sensors (Figure A1b) showed much greater variability. There were two aspects to this. First, there were short periods when dramatic drops in conductivity (and inferred salinity) occurred, which we view as artifacts of supercooling behavior as discussed in section 2. Excluding these periods, it is clear that a sizable offset between the SBE sensors and the RDCP sensor persisted throughout the deployment. Although at the scale shown, the SBE4 conductivity sensors agree reasonably well, the higher-frequency response of the pumped TIC1 SBE4 instrument is suspect as described later. For this reason we placed priority on carefully calibrating the microstructure (SBE7) instrument mounted with TIC1. The SBE7 μC time series calculated using the factory calibrations is included to illustrate that although the mean value is obviously biased low compared with the others, its deviations from the mean are comparable in magnitude to the others.

[44] Based on previous experience, we anticipated that the pumped apparatus in TIC1 would provide adequate frequency response for calculating salinity and buoyancy flux; however, we found upon analysis that the TIC1 conductivity record showed much less high-frequency variation than either the μC or TIC2 (standard SBE4, unpumped) sensors. Furthermore, its response to rapid variation in salinity appeared to noticeably lag in comparison

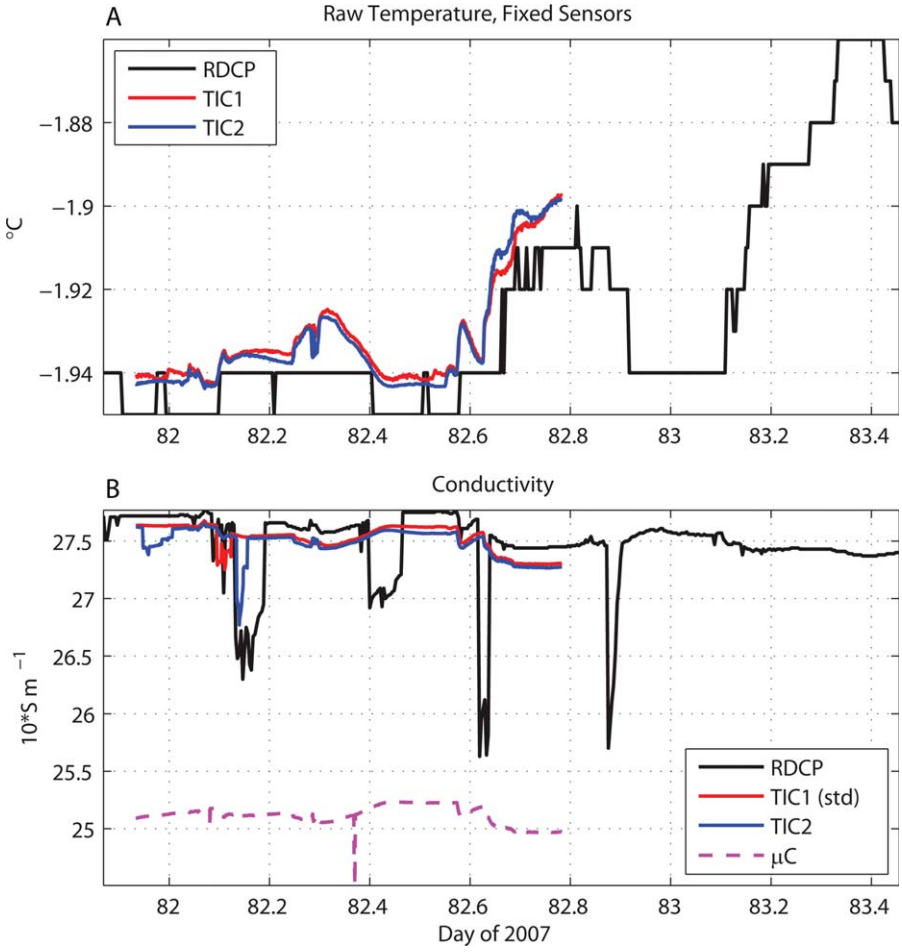

Figure A1. (a) One-minute average raw temperature records from TICs 1 and 2, plus the RDCP. (b) Conductivity from standard (SBE4) conductivity meters for TICs 1 and 2, and RDCP (solid traces), and for the microstructure conductivity sensor with factory calibrations (dashed).

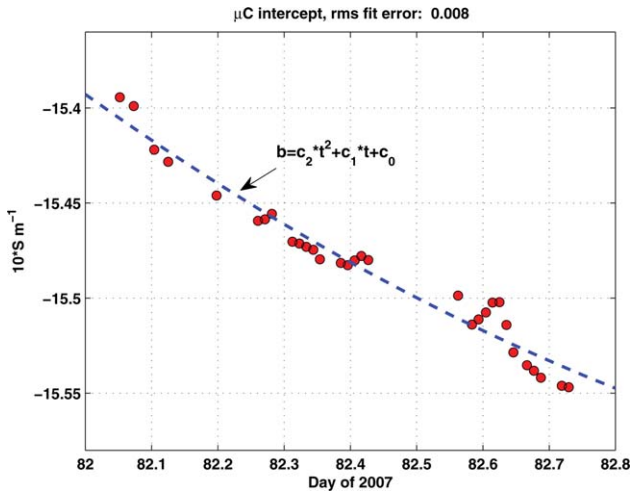

Figure A2. Polynomial fit to μC intercept $b = mf_{\mu C} - C_{TIC2}$, where $f_{\mu C}$ is the realization-average μC frequency, m is the factory calibration slope, and C_{TIC2} is the average conductivity at TIC2, assumed correct.

with the others. For practical purposes, at low temperatures conductivity of both the standard and μC SBE instruments is proportional to the frequency output. By normalizing departure of instrument frequency from the mean by its standard deviation over a suitable averaging interval, we were able to show that maximum lagged correlation between the pumped and μC instruments occurred with a lag of about 25 s. Shifting the pumped time series forward in time by 25 s resulted in reasonably good correspondence with the other two sensors, except for damping of higher-frequency fluctuations. While it is not obvious why the response of the pumped SBE4 instrument lagged both the collocated SBE7 (μC) and the lower (unpumped) SBE4 instruments, we note that in the pumped pair, the plumbing that routes fluid from the thermometer to the conductivity cell includes two right-angle bends. It is possible that enough ice formed and remained in these constrictions to retard flow past the conductivity sensor by the observed lag. During the 2007 exercise, similar deployments were made at two other sites with water temperatures slightly above freezing, both before the FMS study (in Van Mijenfjorden) and after (Barents Sea). In those conditions, we found no evidence of similar lag between the standard SBE4 instrument and collocated μC instruments on TIC1, nor with timing of larger-scale features observed at TIC2, 2 m lower.

[45] The SBE7 μC instruments produce a signal frequency that is related linearly to conductivity over the limited range of conductivities encountered in the study. In previous deployments, μC instruments used in combination with the standard SBE4 conductivity meters have often shown significant drift in absolute calibration [*McPhee and Stanton*, 1996; *McPhee et al*., 2008; *Sirevaag et al*., 2010], in addition to occasional sudden shifts in output frequency. This presents an obvious interpretation problem, particularly in our case where the collocated SBE4 (pumped) conductivity time series appeared to lag the other instruments as described earlier, possibly associated with icing problems. By examining 15 min segments of data during which salinity varied significantly, and for which there were no sudden shifts in μC output, we found that the slope of the linear relation between μC frequency and conductivity at TIC2 was not significantly different from the factory calibration, but that the intercept (i.e., actual calibration) varied more or less predictably over the deployment period (Figure A2), as illustrated by the polynomial fit with time. Consequently, we estimated the actual conductivity at TIC1 as $C_1 = mf_{\mu C} + b(t)$, where $b(t)$ is from the cubic fit.

[46] Apart from the "dropout" events discussed in section 2, there was an obvious offset between the RDCP and TIC2 conductivities (Figure A1). Again assuming C_{TIC2} to be correct, we applied a constant correction to C_{RDCP} (-0.013 S m^{-1}) so that mean values over a common measurement period when there was little change agreed with C_{TIC2}.

[47] **Acknowledgments.** We thank A. Sirevaag for suggesting improvements to this manuscript. Support for this research was provided by National Science Foundation grants ARC-0856214 and ANT-0739371 (M.G.M.) and by the IPY project Bipolar Atlantic Thermohaline Circulation (BIAC) and the Storfjorden Polynya Air Sea Ice Exchange Experiment (POLRES grant 196145) from the Norwegian Research Council (R.S., F.N., and L.H.S.). We thank two anonymous reviewers for helpful comments. We will also thank the captain and crew at the Norwegian coastguard vessel K/V *Svalbard* for superb service and invaluable help during the FMS field campaign.

References

Coachman, L. K. (1966), Production of supercooled water during sea ice formation, in Proceedings of the Symposium on the Arctic Heat Budget and Atmospheric Circulation, Lake Arrowhead, California, 31 January to 4 February 1966, pp. 497–529, Rand Corp., Santa Monica, Calif.

Crawford, G., L. Padman, and M. McPhee (1999), Turbulent mixing in Barrow Strait, *Cont. Shelf Res.*, *19*, 205–245.

Daly, S. F. (1984), *Frazil ice dynamics*, CRREL Monogr. 84–1, U.S. Army Cold Regions Research and Engineering Laboratory, Hanover, NH.

Dempsey, D. E., P. J. Langhorne, N. J. Robinson, M. J. M. Williams, T. G. Haskell, and R. D. Frew (2010), Observation and modeling of platelet ice fabric in McMurdo Sound, Antarctica, *J. Geophys. Res.*, *115*, C01007, doi:10.1029/2008JC005264.

Foldvik, A., and T. Kvinge (1974), Conditional instability of sea water at the freezing point, *Deep Sea Res.*, *21*, 160–174.

Gill, A. E. (1982), *Atmosphere-Ocean Dynamics*, 662 pp., Academic, New York.

Hinze, J. O. (1975), *Turbulence*, 2nd ed., 790 pp., McGraw-Hill, New York.

Krylov, A. D., and A. G. Zatzepin (1992), Frazil ice formation due to difference in heat and salt exchange across a density interface, *J. Mar. Sci.*, *3*, 497–506.

Leonard, G. H., P. Langhorne, M. Williams, R. Vennell, C. Purdie, D. Dempsey, T. Haskell, and R. Frew (2011), Evolution of supercooling under coastal Antarctic sea ice during winter, *Antarct. Sci.*, *23*, 309–409, doi:10.1017/S0954102011000265.

Lewis, E. L., and R. G. Perkin (1983), Supercooling and energy exchange near the Arctic Ocean surface, *J. Geophys. Res.*, *88*(C12), 7681–7685, doi:10.1029/JC088iC12p07681.

McPhee, M. G. (1994), On the turbulent mixing length in the oceanic boundary layer, *J. Phys. Oceanogr.*, *24*, 2014–2031.

McPhee, M. G. (2008), *Air-Ice-Ocean Interaction: Turbulent Ocean Boundary Layer Exchange Processes*, Springer, New York.

McPhee, M. G., and T. P. Stanton (1996), Turbulence in the statically unstable oceanic boundary layer under Arctic leads, *J. Geophys. Res.*, *101*(C3), 6409–6428, doi:10.1029/95JC03842.

McPhee, M. G., R. Kwok, R. Robins, and M. Coon (2005), Upwelling of Arctic pycnocline associated with shear motion of sea ice, *Geophys. Res. Lett.*, *32*, L10616, doi:10.1029/2004GL021819.

McPhee, M. G., J. H. Morison, and F. Nilsen (2008), Revisiting heat and salt exchange at the ice-ocean interface: Ocean flux and modeling considerations, *J. Geophys. Res.*, *113*, C06014, doi:10.1029/2007JC004383.

Mellor, G. L., M. G. McPhee, and M. Steele (1986), Ice-seawater turbulent boundary layer interaction with melting or freezing, *J. Phys. Oceanogr.*, *16*, 1829–1846.

Rippeth, T. P., N. R. Fisher, and J. H. Simpson (2001), The cycle of turbulent dissipation in the presence of tidal straining, *J. Phys. Oceanogr.*, *31*, 2458–2471.

Robinson, N. J., M. J. M. Williams, P. J. Barrett, and A. R. Pyne (2010), Observations of flow and ice-ocean interaction beneath the McMurdo Ice Shelf, Antarctica, *J. Geophys. Res.*, *115*, C03025, doi:10.1029/2008JC005255.

Sirevaag, A., M. G. McPhee, J. H. Morison, W. J. Shaw, and T. P. Stanton (2010), Wintertime mixed layer measurements at Maud Rise, Weddell Sea, *J. Geophys. Res.*, *115*, C02009, doi:10.1029/2008JC005141.

Skogseth, R., L. H. Smedsrud, F. Nilsen, and I. Fer (2008), Observations of hydrography and downflow of brine-enriched shelf water in the Storfjorden polynya, Svalbard, *J. Geophys. Res., 113*, C08049, doi:10.1029/2007JC004452.

Skogseth, R., M. G. McPhee, F. Nilsen, and L. H. Smedsrud (2013), Creation and tidal advection of a cold salinity front in Storfjorden: 1. Polynya dynamics, *J. Geophys. Res. Oceans.*, *118*, C02009, doi:10.1002/jgrc.20231.

Smedsrud, L. H. (2001), Frazil-ice entrainment of sediment: Large-tank laboratory experiments, *J. Glaciol.*, *47*, 461–471.

Steele, M., G. L. Mellor, and M. G. McPhee (1989), Role of the molecular sublayer in the melting or freezing of sea ice, *J. Phys. Oceanogr.*, *19*, 139–147.